

Discovery of a weak topological insulating state and van Hove singularity in triclinic RhBi_2

Kyungchan Lee,^{1,2} Gunnar F. Lange,³ Lin-Lin Wang,^{1,2} Brinda Kuthanazhi,^{1,2}
Thaís V. Trevisan,^{1,2} Na Hyun Jo,^{1,2} Benjamin Schruck,^{1,2} Peter P. Orth,^{1,2}
Robert-Jan Slager,^{3,4,*} Paul C. Canfield,^{1,2,†} and Adam Kaminski^{1,2,‡}

¹*Ames Laboratory, Ames, Iowa 50011, USA*

²*Department of Physics and Astronomy,
Iowa State University, Ames, Iowa 50011, USA*

³*TCM Group, Cavendish Laboratory, University of Cambridge,
Cambridge CB3 0HE, United Kingdom*

⁴*Department of Physics, Harvard University, Cambridge MA 02138, USA*

(Dated: September 22, 2021)

Time reversal symmetric (TRS) invariant topological insulators (TIs) fulfill a paradigmatic role in the field of topological materials, standing at the origin of its development. Apart from TRS protected 'strong' TIs, it was realized early on that more confounding weak topological insulators (WTI) exist. WTIs depend on translational symmetry and exhibit topological surface states only in certain directions making it significantly more difficult to match the experimental success of strong TIs. We here report on the discovery of a WTI state in RhBi_2 that belongs to the optimal space group $\text{P}\bar{1}$, which is the only space group where symmetry indicated eigenvalues enumerate all possible invariants due to absence of additional constraining crystalline symmetries. Our ARPES, DFT calculations, and effective model reveal topological surface states with saddle points that are located in the vicinity of a Dirac point resulting in a van Hove singularity (VHS) along the (100) direction close to the Fermi energy (E_F). Due to the combination of exotic features, this material offers great potential as a material platform for novel quantum effects.

From the perspective of considering solely TRS, 3D topological insulators are classified by a series of \mathbf{Z}_2 topological invariants, $(\nu_0; \nu_1\nu_2\nu_3)$. The case $\nu_0 = 1$ is referred to as a strong topological insulator (STI)^{1,2}. A characteristic feature of a STI is the existence of gapless topological surface state (TSS) on all surfaces, which have been observed experimentally in many materials such as $\text{Bi}_{1-x}\text{Sb}_x$, Bi_2Se_3 , and Bi_2Te_3 ³. In contrast to 2D TIs, even when $\nu_0 = 0$ the system can have non-trivial ν_i , resulting in a weak topological insulator (WTI). Reported WTI states are rather rare as gapless TSS can be detected only on particular surfaces, which may not be natural cleaving planes in many 3D materials. For instance, $\text{Bi}_{14}\text{Rh}_3\text{I}_9$ was predicted to be a WTI with $\mathbf{Z}_2 = (0;001)$. However, experimental verification of the TSS remain elusive since the cleaving plane is (001), which is a topologically trivial side⁴. The recent development of nano-ARPES has reinvigorated the search for WTIs. For instance, a first WTI TSS was only recently measured by isolating a $\sim 2 \mu\text{m}$ size side facet and using nano-ARPES in quasi-one-dimensional bismuth iodide $\beta\text{-Bi}_4\text{I}_4$ ⁵.

As part of an effort to design and discover materials with novel, intrinsically non-trivial, topological properties we identified RhBi_2 as an exciting candidate material. To minimize potential degeneracies in reciprocal space, we decided to start with the lowest possible symmetry unit cell: triclinic. To maximize spin-orbit coupling we chose the heaviest (essentially)

stable element, Bi as a majority component. For simplicity we chose to start by limiting our search to binary compounds. As a result of this cascade of physically inspired constraints we rapidly identified RhBi₂ as a promising candidate material with clear van der Waals-like bonding along the crystallographic *a*-axis (Fig. 1b). Here, we provide theoretical understanding and experimental evidence of the simplest WTI state in triclinic crystal RhBi₂ with clear TSS at the natural cleaving surface. As we will discuss below, the WTI classification of RhBi₂ maximally profits from its space group. As $P\bar{1}$ only features inversion in addition to translations, all topological properties in the presence of TRS can faithfully be determined from the parity eigenvalues of the occupied bands at TRIM points⁶. Moreover, due to the absence of additional symmetries none of these high symmetry momenta are related and a WTI can exist in every stacking direction⁷. In fact, this carefully selected, simple structure makes this the only space group in which the symmetry eigenvalues at TRIM points convey all topological invariants one-to-one⁸⁻¹¹. Rather surprisingly, we find that this freedom of choosing the stacking direction culminates in an index, (0;001), that is perpendicular to the layering of the material, creating the possibility of a TSS preserving cleavage plane.

The lack of symmetries, especially the absence of rotational symmetry, in triclinic RhBi₂ allows the system to have a saddle points, where the curvature of a band has opposite sign in two perpendicular direction in momentum space. A saddle point is closely related to a VHS, leading to a divergence in the density of states. Previously, VHSs have been reported in a variety of materials; graphene^{12,13}, cuprate superconductors¹⁴⁻¹⁶, Pt₂HgSe₃¹⁷, Pb_{1-x}Sn_xSe(Te)¹⁸. The proximity of the E_F to a VHS can significantly enhance quantum many body instabilities and it can drive superconductivity¹⁹⁻²¹ ferromagnetism²²⁻²⁵ and antiferromagnetism²⁶ depending on the topology of the band structure. Owing to the simplest topological classification and VHS in the vicinity of E_F , triclinic crystal RhBi₂ offers unique advantages for exploring exotic quantum phenomena in a weak topological insulator.

We present a study of triclinic RhBi₂ by using ARPES, DFT calculations and an effective model. Our result reveals two surface Dirac points, which are protected by time-reversal symmetry at the $\bar{\Gamma}$ and \bar{Z} points. We focused experimental attention at the momentum space around the \bar{Z} point of the surface BZ. The shape of the Dirac cone around \bar{Z} is significantly modified from typical Dirac dispersion due to the presence of two saddle points associated with a VHS. The saddle points are located at a binding energy of ~ 80 meV. Based on DFT

calculations, we identify that surface state of RhBi_2 along (100) has a WTI phase, which is characterized by $\mathbf{Z}_2=(0;001)$.

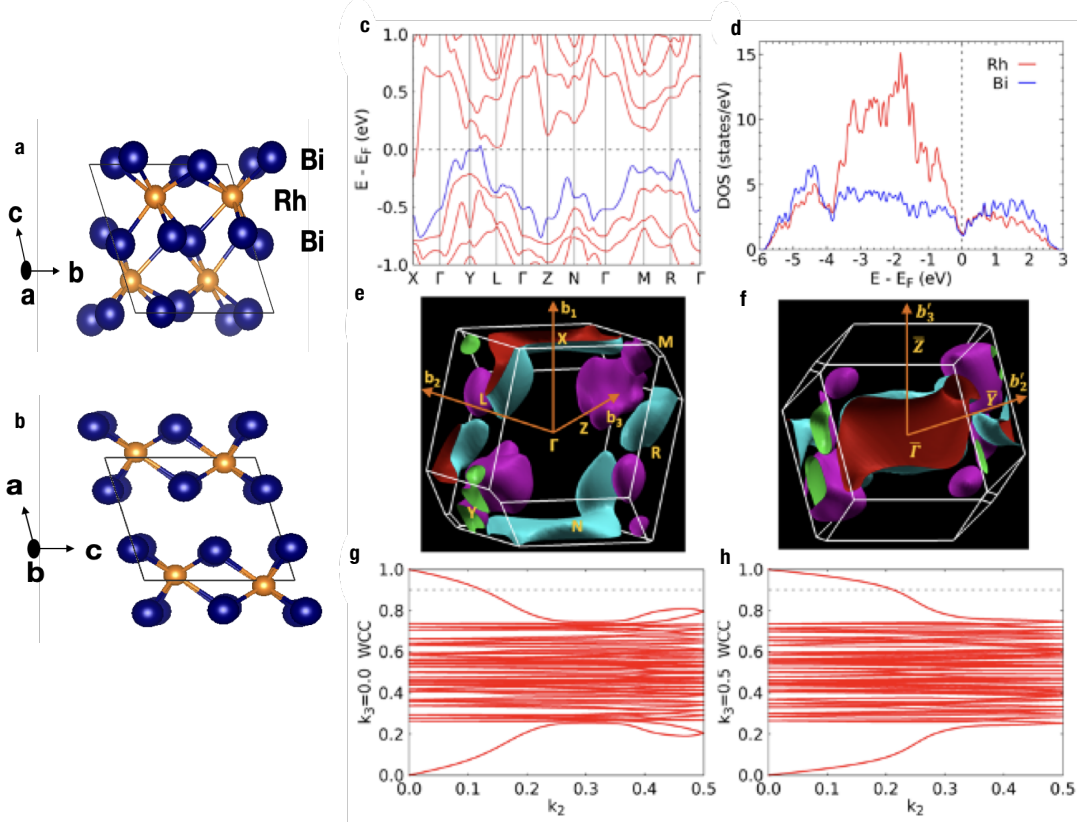


FIG. 1. **Calculated bulk band structure, DOS and WCC evolution of RhBi_2 .** **a-b**, Crystal structure of triclinic RhBi_2 with different orientations (Bi:blue spheres, Rh: yellow spheres). **c**, Bulk band structure of RhBi_2 in the triclinic crystal structure (space group 2) calculated in DFT-PBE with SOC. The top valence band according to electron filling is in blue. **d**, Density of states (DOS) projected on Rh and Bi. **e**, 3D Fermi surface at the (E_F) with eight time-reversal invariant momentum (TRIM) points and reciprocal lattice vectors labeled. Electron and hole pockets are in cyan (red inside) and purple (green inside) respectively. **f**, 3D FS viewed along b_1 axis with projection of TRIM points and 2D reciprocal lattice vectors labeled. **g** and **h**, Wannier charge center (WCC) evolution on the $k_3=0.0$ and 0.5 planes, respectively, showing the non-trivial topology.

Due to the symmetry group hosting only an inversion center, the layered triclinic RhBi_2 is an interesting case in terms of both band structure and topology. The bulk band structure of RhBi_2 calculated from density functional theory^{27,28} (DFT) using PBE exchange correlation functional with spin-orbit coupling (SOC) is plotted in Fig.1c. The 3D FS at the E_F

is shown in Fig. 1e with the eight time-reversal invariant momentum (TRIM) points and reciprocal lattice vectors labeled. By virtue of inversion symmetry and TRS, all bands are doubly degenerated in the BZ due to Kramers theorem. The bands of interest arise by hybridization from Rh d and Bi p orbitals. From the small but finite density of states (DOS) at E_F in Fig. 1d, we see that RhBi₂ is a metal exhibiting non-overlapping pockets. There are no crossings between the top valence and bottom conduction bands anywhere in the BZ. The two bands crossing the E_F give multiple electron and hole pockets. The electron and hole pockets are near BZ boundaries, while there is a large band gap around the BZ center Γ point. Notable are the electron pockets around X and near L points and the hole pockets near the Y point. There are also two small hole pockets totally inside the BZ. Although the structure is stacked on the bc plane along the b_1 direction, a large electron pocket is on the $b_1=0.5$ plane around the X point. In contrast, there is band gap on the $b_3=0.5$ plane around the Z point.

With inversion being the only symmetry in the system besides time-reversal symmetry, the topological features are determined by the parity eigenvalues of the occupied bands at TRIM points⁶. In fact, from the perspective of the recent advancements in classifying band structures using constraints in symmetry eigenvalues⁹ and comparing them to atomic configurations^{10,11}, the space group at hand, number 2 or $P\bar{1}$, is the *only* one in which such symmetry indicators unambiguously define all topological invariants^{7,8}, as there are no symmetry constraints between high symmetry momenta⁷. The topological indices, apart from TRS invariant ν_0 that we find to be zero, comprise three \mathbf{Z}_2 invariants corresponding to the weak indices and a \mathbf{Z}_4 index²⁹ that comes from promoting ν_0 to the inversion symmetric context. The latter corresponds to the twice the value of the inversion invariant δ_i , $\mathbf{Z}_4 = 2\delta_i$, here⁸. The calculated \mathbf{Z}_4 index is 2, indicating that RhBi₂ is topologically non-trivial, but indeed not a strong topological insulator. The calculated parity eigenvalue products are (+1) at Γ and Z points, and (-1) at all the other TRIMs, which gives the Fu-Kane index of (0;001), determining the three \mathbf{Z}_2 invariants. This can also be confirmed by Wannier charge center (WCC) evolution or Wilson loop on $k_3=0.0$ and 0.5 planes in Figs. 1g and g, showing 2D $\mathbf{Z}_2=1$ on these planes³⁰⁻³². In contrast, 2D $\mathbf{Z}_2=0$ on the other $k_{1,2}=0.0$ or 0.5 planes. Interestingly, although the layered structure is stacked along the b_1 direction, the weak TI can be seen as a stacking of quantum spin Hall (QSH) layers along the b_3 direction.

In Fig. 1f, the 3D FS is rotated for the view along b_1 or perpendicular to the bc plane,

i.e. (100). On the (100) surface, the Γ and X points are projected to $\bar{\Gamma}$ point, Z and N to \bar{Z} point, and Y and L to \bar{Y} point, respectively. This shows that for the 2D FS on (100) around the E_F , the area near the \bar{Z} point is gapped without bulk band projection, while the $\bar{\Gamma}$ and \bar{Y} points are surrounded by bulk states. For bulk-boundary correspondence of TIs³³, parity eigenvalue products can also be projected onto surface as in $\pi_a = \delta_{a1} \delta_{a2}$, where TRIM a_1 and a_2 projected into a on surface. The result is (-1) for $\bar{\Gamma}$ and \bar{Z} points, while (+1) for the others. Thus, an even number of two surface Dirac points will emerge on (100), one at $\bar{\Gamma}$ and the other at \bar{Z} . In summary, RhBi₂ is a topologically non-trivial 2D material as a layered compensating semimetal hosting the simplest WTI possible as the underlying space group has minimal symmetry.

In order to verify the nontrivial topological nature of triclinic RhBi₂, we performed ARPES measurements and DFT calculations to identify relevant features in the electronic structure. Fig. 2a shows the FS of triclinic RhBi₂ measured using laser-based APRES, where dashed lines mark main crystallographic directions in the BZ. The measured band dispersion along those lines are shown in Figs. 2b and c. Two Dirac points are clearly present in the data: one located at the $\bar{\Gamma}$ point with a binding energy of ~ 500 meV and the other at the \bar{Z} point with a binding energy of ~ 80 meV. The red arrow marks the Dirac point at the $\bar{\Gamma}$ point and the blue arrow marks the Dirac point at the \bar{Z} point. Fig. 2c shows the band dispersion along the $\bar{\Gamma}$ - \bar{Y} direction where the red arrow marks the location of the Dirac point there. Figs. 2d-f show DFT calculations along the same directions as for the ARPES data. Overall, DFT calculations agree quite well with experimental data. Unlike typical TSS of STIs, which have a single Dirac point, we observe two surface Dirac points at TRIM points. This apparent discrepancy between STIs and WTIs shows that triclinic RhBi₂ possesses TSS arising from weak topological insulating phase in (100) direction. In addition, we observed twofold rotational symmetry at the FS from the DFT calculations, although the crystal structure is triclinic. This is because three-dimensional inversion symmetry reduces to effectively two-dimensional rotation symmetry upon projection of all transverse momenta. To understand this phenomenon, we carefully studied different projections of each layer in the unit cell. Appendix C shows different projections of $k_1(k_x)$ values on (100) surface. Red looped curves represent electron pockets. Based on the calculation, only projections from $k_1 = 0$ and 0.5 planes show twofold rotational symmetry and the $k_1 = 0$ plane shows large electron pocket around the center of the BZ. Therefore, the large electron pocket around $\bar{\Gamma}$

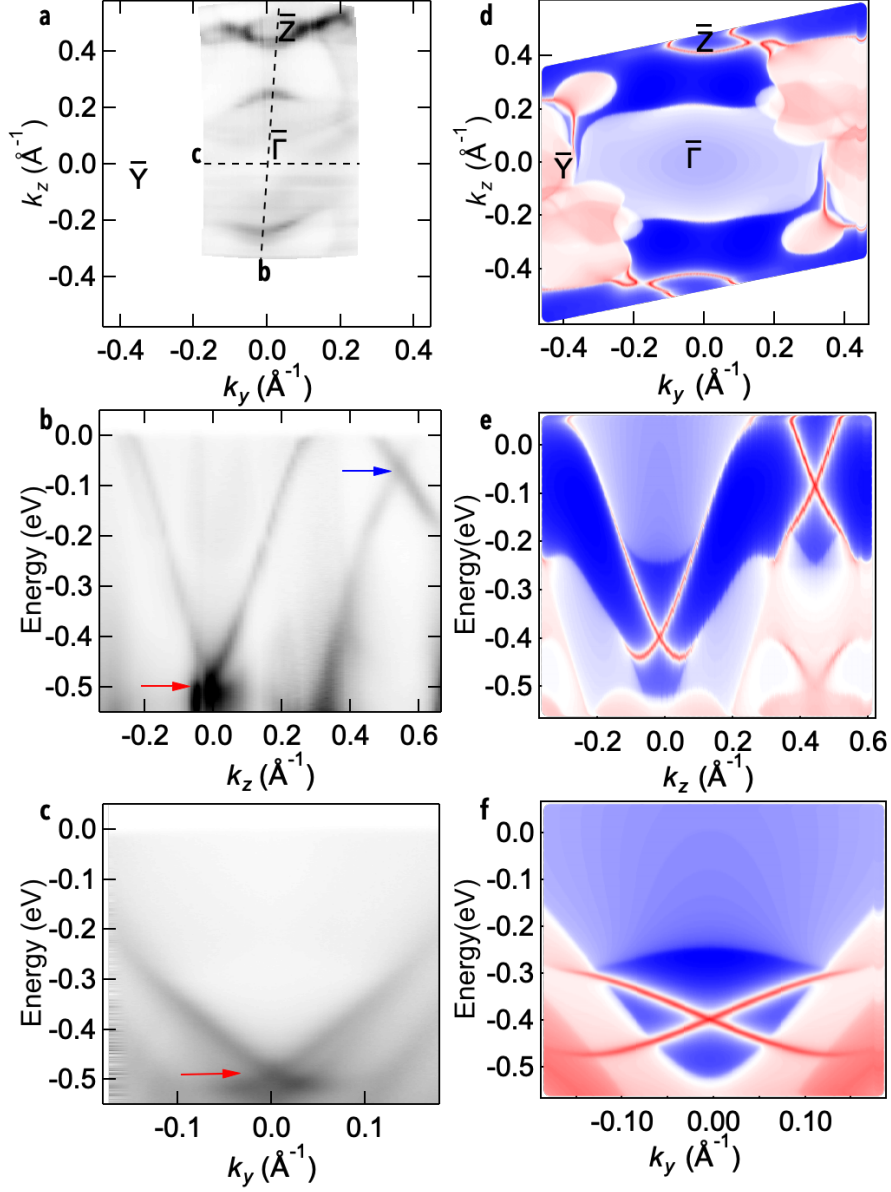


FIG. 2. **Experimental and calculated Fermi surface and band dispersion of RhBi₂ at $T = 40$ K.** **a**, Fermi surface plot of the ARPES intensity integrated within 10 meV of the chemical potential along $\bar{\Gamma}$ - \bar{Z} . **b**, Band dispersion along the $\bar{\Gamma}$ - \bar{Z} line. **c**, Band dispersion along $\bar{\Gamma}$ - \bar{Y} . **d**, DFT calculations of Fermi surface. **e-f**, DFT calculations of energy dispersion corresponding to the ARPES data **b** and **c**, respectively.

is mainly from the $k_1 = 0$ plane and addition of all planes in the BZ will give us the effective twofold rotational symmetry on the 2D FS.

Out of the two surface Dirac points present, the Dirac point around the \bar{Z} point is by far

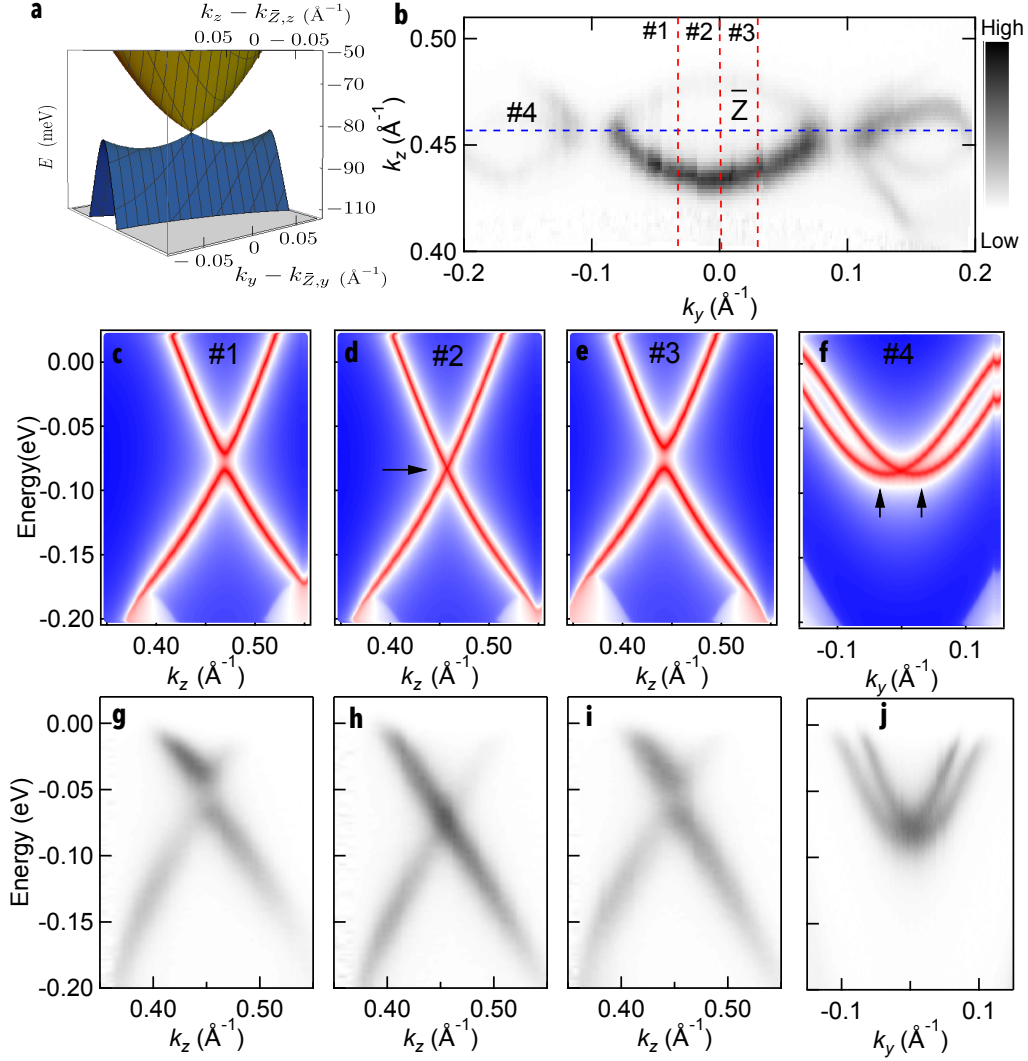


FIG. 3. **Saddle points and Dirac dispersion around the \bar{Z} point.** **a**, $k \cdot p$ model band dispersion around the \bar{Z} point, revealing a nodal point, two saddle points and the almost-flat region of the lower energy band at slightly lower energies. The two saddle points at energy -83 meV are responsible for the logarithmic divergence of the DOS. **b**, Fermi surface plot of the ARPES intensity integrated within 10 meV of the chemical potential around the \bar{Z} point. Dark areas mark location of the FS. **c-f**, Calculated band dispersion along the vertical direction in **b** that is marked as red dashed lines (#1-3), respectively. **f**, Calculated band dispersion along the horizontal direction in **b** that is marked as a blue dashed line (#4). Black arrows mark locations of band minimums. **g-j** ARPES data along the same cuts as in **c-f**.

the more interesting. Instead of a typical Dirac like dispersion³⁴, it shows a strong warping

effect along the energy axis making saddle points in the lower band. $k \cdot p$ model band dispersion in Fig. 3a illustrates the Dirac point and two saddle points that exist in proximity of the \bar{Z} point. The FS in this area of BZ is plotted in Fig. 3b. Figs. 3c-f display calculated DFT band dispersion in the vertical direction(#1-3) and one horizontal cut(#4) which are marked as dashed lines in Fig. 3b. Interestingly, the vertical cuts (along k_z), Figs. 3c-e, show the lower band with negative curvature while the horizontal cut (along k_y), Fig. 3f, shows the lower band with positive curvature. Along cut 4, there are actually two upper bands that give rise to two local minimums in energy as marked by black arrows. Those two minimums give rise to two saddle points as demonstrated in Fig. 3a. In cut 1 we can see the upper and lower band are separated in energy (Fig. 3c). Band dispersion along the $\bar{Z}-\bar{\Gamma}$ line is shown in Fig. 3d. Dirac dispersion is clearly visible with Dirac point at the binding energy of ~ 80 meV and is marked by the black arrow. Figure 3e displays the band dispersion at the cut 3, where the two bands are clearly separated as in cut 1. The separation in Figs. 3c and e is fairly symmetric with respect to the Dirac point. Corresponding ARPES data, measured along the same cuts in the BZ are shown in Figs. 3g-j. Based on calculations and the experimental result, we conclude that this is the surface state forms a Dirac point rather than a line of Dirac dispersion along the k_y direction. On the other hand, band dispersion in the horizontal direction significantly deviates from the vertical directions as shown in Fig. 3f and j. Both upper and lower bands have a parabolic dispersion instead of the linear dispersion. Naturally, the lower band shows positive curvature. As a result, it looks like the overlap of two parabolic bands with slightly different curvatures.

To qualitatively address the observed saddle points in vicinity of the \bar{Z} point on the (100) surface we consider a simple effective model. As we have time-reversal (\mathcal{T}) and inversion symmetry (\mathcal{P}) in the bulk, $\mathcal{A} = \mathcal{PT}$ commutes with Hamiltonian, reflecting the Kramers degeneracy by virtue of squaring to -1 . The presence of this symmetry will constrain the form of the bulk Hamiltonian affecting the effective model for the surface after projecting. This will be reported elsewhere and we simply note that \mathcal{P} is formally broken on the surface. In fact, having the inversion centre at the origin ensures that surface states with opposite \mathcal{P} -value reside on opposite surfaces. Hence, as motivated in SI Appendix B, we consider a simple two-band model that is only constrained by TRS to describe the strongly anisotropic

anomalous edge states,

$$H(\mathbf{k}) = d_0(\mathbf{k})I + d_1(\mathbf{k})\sigma_x + d_2(\mathbf{k})\sigma_y + d_3(\mathbf{k})\sigma_z \quad (1)$$

In the above $d_0(\mathbf{k})$ is even in \mathbf{k} and $d_{1,2,3}(\mathbf{k})$ are odd in \mathbf{k} . Expanding our energy to second order then gives

$$\varepsilon_{\pm}(\mathbf{k}) = E_0 + A_1k_y^2 + A_2k_z^2 + A_3k_yk_z \pm \sqrt{\sum_{i=1}^3 (B_ik_y + C_ik_z)^2}, \quad (2)$$

where E_0 is the energy at the crossing points of the surface bands, $\{A_i\}$, $\{B_i\}$ and $\{C_i\}$ are all real parameters and momenta are measured relative to the \bar{Z} point. To accommodate strain effects, we could also expand $H(\mathbf{k})$ to third order, giving:

$$\varepsilon_{3\pm}(\mathbf{k}) = E_0 + A_1k_y^2 + A_2k_z^2 + A_3k_yk_z \pm \sqrt{\sum_{i=1}^3 (B_ik_y + C_ik_z + D_ik_y^2k_z + E_ik_yk_z^2)^2} \quad (3)$$

We use simulated annealing to fit this model to our surface band structure around the \bar{Z} point. This gives the parameters shown in table I and II in SI appendix B. Note that our parameter space is very high dimensional, so we cannot hope to find the physically relevant parameters. This will be rectified in a future work. As we here are interested only in an effective model to compute the DOS, and as we have the full DFT results available, any model which reproduces the energy dispersion close to the crossing point is sufficient.

Extrema of the energy dispersion, $\nabla\varepsilon_{\mathbf{k}} = 0$, are called van Hove points and lead to singularities in the density of states (DOS): $g(E) = g_s \int \frac{d^{d-1}k}{(2\pi)^d} \frac{1}{|\nabla\varepsilon_{\mathbf{k}}|_{\varepsilon_{\mathbf{k}}=E}}$ (g_s denotes spin degeneracy). In two dimensions, $d = 2$, saddle points of the dispersion lead to a logarithmically divergent DOS. If this divergence occurs close to the Fermi energy, electronic correlations are strongly amplified, which can drive the system towards various electronically ordered states such as superconductivity, spin or charge density waves. In contrast, nodal points of the dispersion, where the Fermi surface shrinks to a point are characterized by a vanishing DOS.

As described above, our ARPES measurements indicate the presence of both van Hove and nodal points in the surface bands of RhBi_2 that occur in close proximity to each other. To further underpin this observation, we here study in detail the properties of a low-energy $k \cdot p$ model (see Eq. (2)) that describes the band structure around the \bar{Z} point in the surface BZ

(sBZ). As shown in Fig. 3a, the surface band structure exhibits a nodal point at the \bar{Z} point, $(k_{\bar{z},y}, k_{\bar{z},z}) = (0, 0.5)\frac{\pi}{a}$. At this point the singly degenerate lower and upper bands touch at an energy $E = -80$ meV below the Fermi energy $E_F = 0$. Both bands are anisotropic away from the nodal point due to the low symmetry of the material. This is particularly noticeable in the lower band, where the dispersion along the direction $k_y - k_{\bar{z},y} = -4.15(k_z - k_{\bar{z},z})$ is almost flat and quadratic, while it is much steeper in the orthogonal direction (see Fig.S4 in the SI). Importantly, the lower band features two saddle points near \bar{Z} at $(k_y, k_z) \approx (-0.042, 0.510)\frac{\pi}{a}$ and $(0.042, 0.490)\frac{\pi}{a}$. The saddle points reside at energy $E = -85$ meV, which is only 3 meV below the energy of the nodal point. As shown in Fig. 4a, this gives rise to an intriguing density of states with a logarithmic divergence in close proximity to a zero. Finally, below the logarithmic singularity ($E < -85$ meV), the DOS is large and almost constant, corresponding to an effective mass of about $m^* \approx 0.4m_e$. This is an average of the almost-flat character of the lower band along $k_y - k_{\bar{z},y} = -4.15(k_z - k_{\bar{z},z})$ and the much steeper dispersion in the orthogonal direction.

To explore one of the possible consequences of the logarithmic divergence in the surface DOS, we calculate the enhancement of a hypothetical superconducting transition temperature T_c . For this purpose, we assume that a fully gapped *s*-wave superconducting state with a transition temperature $T_{c,0}$ is stabilized on the surface of RhBi₂ and we calculate the ratio $T_c/T_{c,0}$ as the system is tuned across the van Hove singularity. A discussion of the microscopic origin of superconductivity and possible other pairing channels is left for future work. Note that similar enhancements are expected in other interaction channels such as for density wave states.

Here, we focus on the weak coupling regime, where T_c can be calculated from the standard BCS expression

$$1 = g \int_{-\Lambda}^{\Lambda} d\xi \frac{\rho(\xi)}{2\xi} \tanh\left(\frac{\xi}{2T_c}\right), \quad (4)$$

where g is a momentum-independent superconducting coupling, which is non-zero only inside an energy window of 2Λ around to the Fermi level. Note that in the case of phonon-mediated superconductivity, Λ corresponds to the Debye frequency. Here, it has a more general meaning, as it denotes an energy cutoff for the effective superconducting coupling that could be mediated either by lattice vibrations (conventional pairing mechanism) or by the electrons themselves (unconventional pairing mechanism).

In the following, we set the Fermi level at the saddle points of the lower band, where the DOS diverges as $\rho(\xi) = \rho_0 \log(D/|\xi|)$, with $\rho_0 \approx 3.2 \times 10^{-3} \text{ \AA}^{-2} \text{eV}^{-1}$ and $D \approx 16.5 \text{ meV}$. As a consequence, a large number of states in the vicinity of \bar{Z} are available to pair with their time-reversed partners around $-\bar{Z}$ favoring a superconducting instability³⁵. Besides the apparent complication due to the logarithmic divergence of the DOS, Eq.(4) can be analytically solved to yield a superconducting transition temperature of

$$T_c \approx 1.13 D e^{-1/\sqrt{\lambda}}. \quad (5)$$

The quantity $\lambda = g\rho_0/2 < 1$ denotes a dimensionless superconducting coupling. Details about the derivation of Eq. (5) can be found in SI Appendix D Sec I. The hypothetical transition temperature T_c is largely enhanced as compared to the standard BCS transition temperature $T_{c,0} \approx 1.13 \Lambda e^{-1/\lambda}$, which is obtained from Eq. (4) for a DOS that can be approximated by a constant. This follows from the fact that Eq. (5) depends on the dimensionless superconducting coupling λ through $e^{-1/\sqrt{\lambda}}$ instead of $e^{-1/\lambda}$. Since $\lambda < 1$ in the weak coupling regime, this causes $T_c/T_{c,0} \gg 1$ as shown in Fig.4(b). Another (subleading) factor that contributes to the enhancement of T_c is that Eq. (5) is proportional to D rather than Λ . Importantly $1/D$ gives the width of the DOS peak, i.e a larger D corresponds to a sharper logarithmic divergence, and typically $D > \Lambda$ ³⁶.

Our results identify RhBi₂ as a very promising topological material that has a Dirac surface state with two saddle points close to E_F . DFT calculations and symmetry analysis show that triclinic RhBi₂ is a weak topological insulator having the simplest space group as reflected in its topological characterization. Based on the effective model, we show that the saddle point is related to a VHS. The proximity of the VHS to the Fermi level also provides opportunities to explore quantum many body instabilities to its inherent susceptibility to such instabilities. Our effective model and DFT calculations present guidance for understanding the saddle points and VHS around the Fermi level.

Apart from the discussed implications, RhBi₂ also hosts potential for other future pursuits. For example, the material could host intriguing new physical phenomena and new topological phase transitions when stress or strain are applied. On a related note, being a WTI in simplest form, RhBi₂ could also spark interest in making it a material platform to examine the role of defects. Indeed, growing a dislocation in different directions will ensure the binding of topologically protected modes when the weak index vector is parallel to the

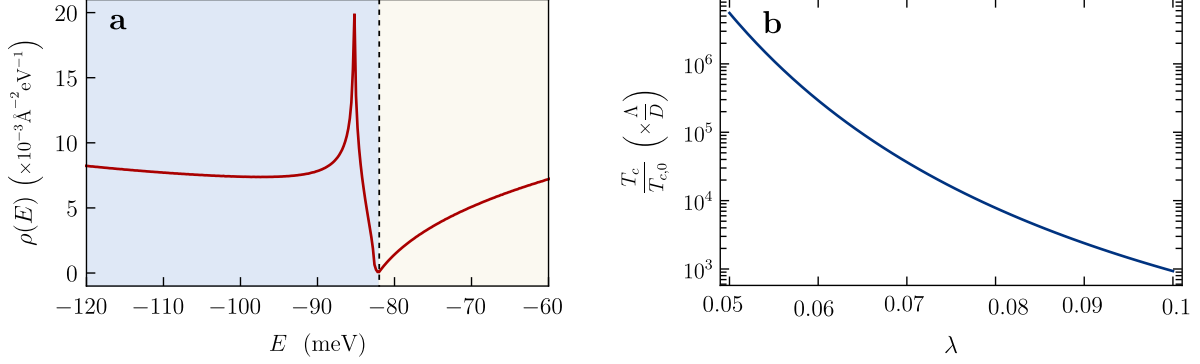


FIG. 4. **a**, Density of states (DOS) of the $k \cdot p$ model describing the surface bands of RhBi₂ in the vicinity of the \bar{Z} point (with coordinates $k_{\bar{Z},y}$ and $k_{\bar{Z},z}$) of the surface Brillouin zone. The DOS from states around \bar{Z} exhibits a logarithmic divergence at $E = -85$ meV and vanishes at $E = -83$ meV. It is almost constant for energies $E < -85$ meV. Here, all energies are with respect to the Fermi energy at $E_F = 0$. **b**, Enhancement of the superconducting transition temperature $T_c/T_{c,0}$ at the van Hove singularity as a function of the bare dimensionless superconducting coupling $\lambda = g\rho_0/2$ in the weak-coupling regime. Here, $T_{c,0}$ corresponds to the standard superconducting transition temperature obtained with a constant DOS at the Fermi level, while T_c is the transition temperature due to a logarithmically divergent DOS at the Fermi level. T_c is normalized by D , while $T_{c,0}$ is normalized by the cutoff Λ .

defect's Burger vector^{37–39}. This pursuit is further underpinned by the unusual nature of the stacking vector (001;0) that is perpendicular to layering of the material and thus poses new relative orientations between the two, directly affecting the possibility of growing defects.

REFERENCES

- * rjs269@cam.ac.uk
- † canfield@ameslab.gov
- ‡ adamkam@ameslab.gov
- ¹ M Zahid Hasan and Charles L Kane, “Colloquium: topological insulators,” *Reviews of modern physics* **82**, 3045 (2010).
 - ² Xiao-Liang Qi and Shou-Cheng Zhang, “Topological insulators and superconductors,” *Rev. Mod. Phys.* **83**, 1057–1110 (2011).
 - ³ Baiqing Lv, Tian Qian, and Hong Ding, “Angle-resolved photoemission spectroscopy and its application to topological materials,” *Nature Reviews Physics* **1**, 609–626 (2019).
 - ⁴ Bertold Rasche, Anna Isaeva, Michael Ruck, Sergey Borisenko, Volodymyr Zabolotnyy, Bernd Büchner, Klaus Koepernik, Carmine Ortix, Manuel Richter, and Jeroen Van Den Brink, “Stacked topological insulator built from bismuth-based graphene sheet analogues,” *Nature materials* **12**, 422–425 (2013).
 - ⁵ Ryo Noguchi, T Takahashi, K Kuroda, M Ochi, T Shirasawa, M Sakano, C Bareille, M Nakayama, MD Watson, K Yaji, *et al.*, “A weak topological insulator state in quasi-one-dimensional bismuth iodide,” *Nature* **566**, 518–522 (2019).
 - ⁶ Liang Fu, Charles L Kane, and Eugene J Mele, “Topological insulators in three dimensions,” *Physical review letters* **98**, 106803 (2007).
 - ⁷ Robert-Jan Slager, Andrej Mesaros, Vladimir Juričić, and Jan Zaanen, “The space group classification of topological band-insulators,” *Nature Physics* **9**, 98–102 (2013).
 - ⁸ Zhida Song, Tiantian Zhang, Zhong Fang, and Chen Fang, “Quantitative mappings between symmetry and topology in solids,” *Nature Communications* **9**, 3530 (2018).
 - ⁹ Jorrit Kruthoff, Jan de Boer, Jasper van Wezel, Charles L. Kane, and Robert-Jan Slager, “Topological classification of crystalline insulators through band structure combinatorics,” *Phys. Rev. X* **7**, 041069 (2017).
 - ¹⁰ Barry Bradlyn, L. Elcoro, Jennifer Cano, M. G. Vergniory, Zhijun Wang, C. Felser, M. I. Aroyo, and B. Andrei Bernevig, “Topological quantum chemistry,” *Nature* **547**, 298–305 (2017).

- ¹¹ Hoi Chun Po, Ashvin Vishwanath, and Haruki Watanabe, “Symmetry-based indicators of band topology in the 230 space groups,” *Nature Communications* **8**, 50 (2017).
- ¹² Guohong Li, A Luican, JMB Lopes Dos Santos, AH Castro Neto, A Reina, J Kong, and EY Andrei, “Observation of van hove singularities in twisted graphene layers,” *Nature Physics* **6**, 109–113 (2010).
- ¹³ Jessica L McChesney, Aaron Bostwick, Taisuke Ohta, Thomas Seyller, Karsten Horn, J González, and Eli Rotenberg, “Extended van hove singularity and superconducting instability in doped graphene,” *Physical review letters* **104**, 136803 (2010).
- ¹⁴ CC Tsuei, DM News, CC Chi, and PC Pattnaik, “Anomalous isotope effect and van hove singularity in superconducting cu oxides,” *Physical review letters* **65**, 2724 (1990).
- ¹⁵ K Gofron, JC Campuzano, H Ding, C Gu, R Liu, B Dabrowski, BW Veal, W Cramer, and G Jennings, “Occurrence of van Hove singularities in $\text{YBa}_2\text{Cu}_4\text{O}_8$ and $\text{YBa}_2\text{Cu}_3\text{O}_{6.9}$,” *Journal of Physics and Chemistry of Solids* **54**, 1193–1198 (1993).
- ¹⁶ Jian Ma, C Quitmann, RJ Kelley, P Alm eras, H Berger, G Margaritondo, and M Onellion, “Observation of a van Hove singularity in $\text{Bi}_2\text{Sr}_2\text{CaCu}_2\text{O}_{8+x}$ with angle-resolved photoemission,” *Physical Review B* **51**, 3832 (1995).
- ¹⁷ Barun Ghosh, Sougata Mardanya, Bahadur Singh, Xiaoting Zhou, Baokai Wang, Tay-Rong Chang, Chenliang Su, Hsin Lin, Amit Agarwal, and Arun Bansil, “Saddle-point Van Hove singularity and dual topological state in Pt_2HgSe_3 ,” *Physical Review B* **100**, 235101 (2019).
- ¹⁸ Madhab Neupane, Su-Yang Xu, R Sankar, Q Gibson, YJ Wang, I Belopolski, N Alidoust, G Bian, PP Shibayev, DS Sanchez, *et al.*, “Topological phase diagram and saddle point singularity in a tunable topological crystalline insulator,” *Physical Review B* **92**, 075131 (2015).
- ¹⁹ JE Hirsch and DJ Scalapino, “Enhanced superconductivity in quasi two-dimensional systems,” *Physical review letters* **56**, 2732 (1986).
- ²⁰ W Kohn and JM Luttinger, “New mechanism for superconductivity,” *Physical Review Letters* **15**, 524 (1965).
- ²¹ Carsten Honerkamp and Manfred Salmhofer, “Magnetic and superconducting instabilities of the hubbard model at the van hove filling,” *Physical Review Letters* **87**, 187004 (2001).
- ²² J González, F Guinea, and MAH Vozmediano, “Kinematics of electrons near a van hove singularity,” *Physical review letters* **84**, 4930 (2000).
- ²³ Angelo Ziletti, Shin Ming Huang, David F Coker, and Hsin Lin, “Van hove singularity and

- ferromagnetic instability in phosphorene,” *Physical Review B* **92**, 085423 (2015).
- ²⁴ Marcus Fleck, Andrzej M Oleś, and Lars Hedin, “Magnetic phases near the van hove singularity in s-and d-band hubbard models,” *Physical Review B* **56**, 3159 (1997).
- ²⁵ R Hlubina, Sandro Sorella, and F Guinea, “Ferromagnetism in the two dimensional t-t’ hubbard model at the van hove density,” *Physical review letters* **78**, 1343 (1997).
- ²⁶ P Lederer, G Montambaux, and D Poilblanc, “Antiferromagnetism and superconductivity in a quasi two-dimensional electron gas. scaling theory of a generic hubbard model,” *Journal de Physique* **48**, 1613–1618 (1987).
- ²⁷ Pierre Hohenberg and Walter Kohn, “Inhomogeneous electron gas,” *Physical review* **136**, B864 (1964).
- ²⁸ Walter Kohn and Lu Jeu Sham, “Self-consistent equations including exchange and correlation effects,” *Physical review* **140**, A1133 (1965).
- ²⁹ Eslam Khalaf, Hoi Chun Po, Ashvin Vishwanath, and Haruki Watanabe, “Symmetry indicators and anomalous surface states of topological crystalline insulators,” *Phys. Rev. X* **8**, 031070 (2018).
- ³⁰ Rui Yu, Xiao Liang Qi, Andrei Bernevig, Zhong Fang, and Xi Dai, “Equivalent expression of F_2 topological invariant for band insulators using the non-abelian berry connection,” *Phys. Rev. B* **84**, 075119 (2011).
- ³¹ A. Alexandradinata, Xi Dai, and B. Andrei Bernevig, “Wilson-loop characterization of inversion-symmetric topological insulators,” *Phys. Rev. B* **89**, 155114 (2014).
- ³² Adrien Bouhon, Annica M. Black-Schaffer, and Robert-Jan Slager, “Wilson loop approach to fragile topology of split elementary band representations and topological crystalline insulators with time-reversal symmetry,” *Phys. Rev. B* **100**, 195135 (2019).
- ³³ Robert-Jan Slager, Louk Rademaker, Jan Zaanen, and Leon Balents, “Impurity-bound states and green’s function zeros as local signatures of topology,” *Phys. Rev. B* **92**, 085126 (2015).
- ³⁴ Yuqi Xia, Dong Qian, David Hsieh, L Wray, Arijeet Pal, Hsin Lin, Arun Bansil, DHYS Grauer, Yew San Hor, Robert Joseph Cava, *et al.*, “Observation of a large-gap topological-insulator class with a single dirac cone on the surface,” *Nature physics* **5**, 398–402 (2009).
- ³⁵ JE Hirsch and DJ Scalapino, “Enhanced superconductivity in quasi two-dimensional systems,” *Physical review letters* **56**, 2732 (1986).
- ³⁶ J Labbe and J Bok, “Superconductivity in alkaline-earth-substituted La_2CuO_4 : a theoretical

- model,” *EPL (Europhysics Letters)* **3**, 1225 (1987).
- ³⁷ Ying Ran, Yi Zhang, and Ashvin Vishwanath, “One-dimensional topologically protected modes in topological insulators with lattice dislocations,” *Nature Physics* **5**, 298–303 (2009).
- ³⁸ Robert-Jan Slager, Andrej Mesaros, Vladimir Juričić, and Jan Zaanen, “Interplay between electronic topology and crystal symmetry: Dislocation-line modes in topological band insulators,” *Phys. Rev. B* **90**, 241403 (2014).
- ³⁹ Jeffrey C. Y. Teo and C. L. Kane, “Topological defects and gapless modes in insulators and superconductors,” *Phys. Rev. B* **82**, 115120 (2010).
- ⁴⁰ Paul C Canfield, “New materials physics,” *Reports on Progress in Physics* **83**, 016501 (2019).
- ⁴¹ Paul C Canfield, Tai Kong, Udharma S Kaluarachchi, and Na Hyun Jo, “Use of frit-disc crucibles for routine and exploratory solution growth of single crystalline samples,” *Philosophical magazine* **96**, 84–92 (2016).
- ⁴² Rui Jiang, Daixiang Mou, Yun Wu, Lunan Huang, Colin D McMillen, Joseph Kolis, Henry G Giesber III, John J Egan, and Adam Kaminski, “Tunable vacuum ultraviolet laser based spectrometer for angle resolved photoemission spectroscopy,” *Review of Scientific Instruments* **85**, 033902 (2014).
- ⁴³ John P Perdew, Kieron Burke, and Matthias Ernzerhof, “Generalized gradient approximation made simple,” *Physical review letters* **77**, 3865 (1996).
- ⁴⁴ Peter E Blöchl, “Projector augmented-wave method,” *Physical review B* **50**, 17953 (1994).
- ⁴⁵ Georg Kresse and Jürgen Furthmüller, “Efficient iterative schemes for ab initio total-energy calculations using a plane-wave basis set,” *Physical review B* **54**, 11169 (1996).
- ⁴⁶ Georg Kresse and Jürgen Furthmüller, “Efficiency of ab-initio total energy calculations for metals and semiconductors using a plane-wave basis set,” *Computational materials science* **6**, 15–50 (1996).
- ⁴⁷ Hendrik J Monkhorst and James D Pack, “Special points for brillouin-zone integrations,” *Physical review B* **13**, 5188 (1976).
- ⁴⁸ Nicola Marzari and David Vanderbilt, “Maximally localized generalized wannier functions for composite energy bands,” *Physical review B* **56**, 12847 (1997).
- ⁴⁹ Ivo Souza, Nicola Marzari, and David Vanderbilt, “Maximally localized wannier functions for entangled energy bands,” *Physical Review B* **65**, 035109 (2001).
- ⁵⁰ Nicola Marzari, Arash A Mostofi, Jonathan R Yates, Ivo Souza, and David Vanderbilt, “Max-

- imally localized wannier functions: Theory and applications,” *Reviews of Modern Physics* **84**, 1419 (2012).
- ⁵¹ DH Lee and JD Joannopoulos, “Simple scheme for surface-band calculations. i,” *Physical Review B* **23**, 4988 (1981).
- ⁵² DH Lee and JD Joannopoulos, “Simple scheme for surface-band calculations. ii. the green’s function,” *Physical Review B* **23**, 4997 (1981).
- ⁵³ MP Lopez Sancho, JM Lopez Sancho, and J Rubio, “Quick iterative scheme for the calculation of transfer matrices: application to mo (100),” *Journal of Physics F: Metal Physics* **14**, 1205 (1984).
- ⁵⁴ MP Lopez Sancho, JM Lopez Sancho, JM Lopez Sancho, and J Rubio, “Highly convergent schemes for the calculation of bulk and surface green functions,” *Journal of Physics F: Metal Physics* **15**, 851 (1985).
- ⁵⁵ QuanSheng Wu, ShengNan Zhang, Hai-Feng Song, Matthias Troyer, and Alexey A Soluyanov, “Wanniertools: An open-source software package for novel topological materials,” *Computer Physics Communications* **224**, 405–416 (2018).

METHODS

RhBi₂ crystals were grown using the high temperature solution growth method out of excess Bi⁴⁰. An initial concentration, Rh₂₀Bi₈₀, of elemental Rh and Bi was placed into a fritted alumina crucible⁴¹ and sealed in fused silica ampoule under a partial pressure of argon. The ampoule was then heated up to 900 °C over 4 hours, held there for 3 hours and cooled down to 480 °C over 200 hours. At this temperature the excess solution was separated from the RhBi₂ crystals using a centrifuge⁴⁰.

ARPES measurements were carried out using a laboratory based tunable VUV laser. The ARPES system consists of a Scienta DA30 electron analyzer, picosecond Ti:Sapphire oscillator and fourth-harmonic generator⁴². All data were collected with 6.7 eV photon energy. Angular resolution was set at $\sim 0.1^\circ$ and 1° , respectively, and the energy resolution was set at 2 meV. The size of the photon beam on the sample was $\sim 30 \mu\text{m}$. Samples were cleaved *in-situ* at a base pressure lower than 1×10^{-10} Torr, 40 K and kept at the cleaving temperature throughout the measurement.

Band structure with spin-orbit coupling (SOC) in density functional theory^{27,28} (DFT) have been calculated with PBE⁴³ exchange-correlation functional, a plane-wave basis set and projected augmented wave method⁴⁴ as implemented in VAS^{45,46}. The experimental lattice parameters in the triclinic unit cell are used. A Monkhorst-Pack⁴⁷ ($7 \times 7 \times 7$) k -point mesh with a Gaussian smearing of 0.05 eV including the Γ point and a kinetic energy cutoff of 229 eV have been used. To calculate topological properties, a tight-binding model based on maximally localized Wannier functions⁴⁸⁻⁵⁰ was constructed to reproduce closely the bulk band structure including SOC in the range of $E_F \pm 1\text{eV}$ with Rh sd and Bi p orbitals. Then the spectral functions and Fermi surface of a semi-infinite RhBi₂ (100) surface were calculated with the surface Green's function methods⁵¹⁻⁵⁴ as implemented in WannierTools⁵⁵.

DATA AVAILABILITY

Relevant data for the work are available at the Materials Data Facility Ref. XX

ACKNOWLEDGEMENTS

We are grateful to Thomas Iadecola for useful discussions and Sergey L. Bud'ko for help with transport measurements. This work was supported by the U.S. Department of Energy, Office of Basic Energy Sciences, Division of Materials Sciences and Engineering. R.-J. S. acknowledges funding from Trinity college, the Marie Curie programme under EC Grant agreement No. 842901 and the Winton programme at the University of Cambridge. G.F.L acknowledges funding from the Aker Scholarship. The research (K.L., L.-L.W, B.K., T.V.T., N.H.J., P.P.O., P.C.C., and A.K.) was performed at Ames Laboratory. Ames Laboratory is operated for the U.S. Department of Energy by the Iowa State University under Contract No. DE-AC02-07CH11358. This work was also supported by the Center for Advancement of Topological Semimetals (B.K., T.V.T., N.H.J., P.P.O.), an Energy Frontier Research Center funded by the U.S. Department of Energy Office of Science, Office of Basic Energy Sciences, through the Ames Laboratory under its Contract No. DE-AC02-07CH11358.

AUTHOR CONTRIBUTIONS

G.F.L, T.V.T., P.P.O and R.-J.S provided theoretical modelling and interpretation. B.K. and P.C.C. designed, grew and characterized the samples. L.-L.W. performed DFT calculations. K.L., N.H.J., B.S., and A.K. performed ARPES measurements and support. The manuscript was drafted by K.L., G.F.L., L.-L.W., B.K., T.V.T., N.H.J., P.P.O., R.-J.S., P.C.C. and A.K. All authors discussed and commented on the manuscript.

COMPETING INTERESTS

The authors declare no competing interests.

SUPPLEMENTARY INFORMATION: DISCOVERY OF A WEAK TOPOLOGICAL INSULATING STATE AND VAN HOVE SINGULARITY IN TRICLINIC RhBi_2

APPENDIX A: CRYSTAL GROWTH AND CHARACTERIZATION

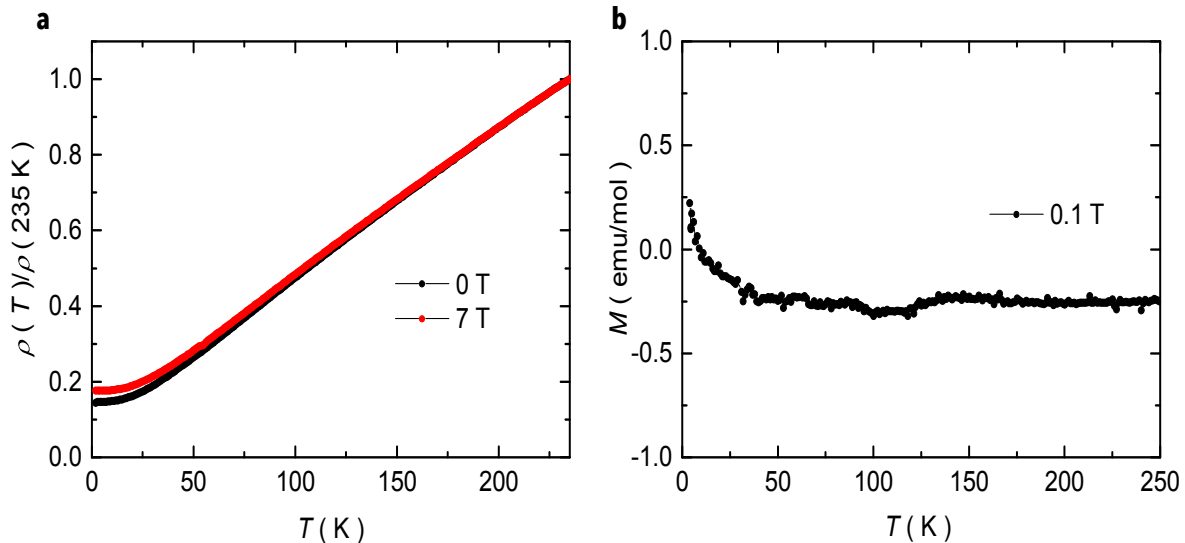


FIG. 5. **Resistivity and magnetization data for RhBi_2 .** **a**, Resistivity data measured in zero field and 7 T. **b**, magnetization measured as a function of temperature in 0.1 T field.

Resistivity as a function of temperature was measured with current in the bc -plane, along one of the crystallographic axis. $\rho(T)$ shows clear metallic behavior with no features that would suggest any sort of phase transition in the measured temperature range. With an applied field of 7 T, $\rho(T)$ do not show any significance changes, except slightly higher resistance values at low temperatures. This very small magnetoresistance is not inconsistent with the relatively low RRR value (~ 6) of the sample. Magnetization as a function of temperature, $M(T)$, was measured with field applied perpendicular to the a -axis, and shows nearly temperature independent behavior, with a small, negative value of M over most of the temperature range. This fundamentally diamagnetic response is consistent with a very small density of states at the Fermi energy resulting in a larger core diamagnetic component.

APPENDIX B: DETAILS OF THE EFFECTIVE MODEL

We aim to build an effective model for the observed surface state close to the \bar{Z} point. As we know the form of the symmetries in the bulk, it would perhaps be most transparent to build a bulk model, which we then explicitly break to the relevant surface. In this section, we discuss this approach and explain why we instead opt to build a surface Hamiltonian directly. We also discuss the construction of this surface Hamiltonian.

A. From bulk model to surface model

A minimal bulk Hamiltonian requires four bands, due to the presence of doubly degenerate bulk Kramer's pairs. A general four-band model can be written in terms of 5 Γ matrices, and their corresponding commutators. However, we can restrict our model by imposing the bulk symmetries. The bulk has inversion and time-reversal symmetry. Combining these gives an operator $\mathcal{A} = \Theta\mathcal{P}$ which satisfies:

$$\mathcal{A}H(\mathbf{k})\mathcal{A}^{-1} = H(\mathbf{k}) \quad (6)$$

We can choose our Γ -matrices to commute with the \mathcal{A} operator[?]. Requiring this gives that the commutators are all zero, so the effective model can be written using only the 5 Γ -matrices. We can represent our symmetry operations as[?]:

$$\mathcal{P} = \sigma_x \otimes I, \quad \Theta = i(I \otimes s_y)\mathcal{K} \quad (7)$$

Where \mathcal{K} is complex conjugation. This gives the 5 Γ -matrices commuting with \mathcal{A} and satisfying the Clifford algebra as:

$$\Gamma^{(1,2,3,4,5)} = \{\sigma_x \otimes I, \sigma_y \otimes I, \sigma_z \otimes s_x, \sigma_z \otimes s_y, \sigma_z \otimes s_z\} \quad (8)$$

Note that Γ^1 equals \mathcal{P} . We can then expand the Hamiltonian as:

$$H(\mathbf{k}) = \epsilon I_{4 \times 4} + M\Gamma^1 + \sum_{i=2}^5 A_i \Gamma_i = \epsilon I_{4 \times 4} + M\Gamma^1 + S \quad (9)$$

Now we note that:

$$\Theta\Gamma^a\Theta^{-1} = \mathcal{P}\Gamma^a\mathcal{P}^{-1} = \begin{cases} 1 & \text{if } a = 1 \\ -1 & \text{if } a \neq 1 \end{cases} \quad (10)$$

From which it follows that ϵ and M are even in $\mathbf{k} \rightarrow -\mathbf{k}$, whereas the $\{A_i\}$ are odd. Furthermore, S anticommutes with Γ^1 , which which it follows that:

$$\mathcal{P}H(k)\mathcal{P}^{-1} = \Gamma_1 H(k) \Gamma_1 = \epsilon I_{4 \times 4} + M \Gamma_1 - S \quad (11)$$

To get the surface states from this bulk Hamiltonian, we organize our Hamiltonian into a term H_0 which contains constants and k_x dependent terms, and a perturbation H_1 which does not contain any k_x dependence. As there is no preferred direction under the symmetry operations, H_0 contains all 5 Γ -matrices, and is therefore not block diagonal. We can then in principle solve H_0 on a finite slab geometry, which would give us four states, two of which are regular on the boundary. These can be interpreted as the edge states. From equation 11, it follows that the opposite parity states will be associated with an opposite sign for matrix S . Explicitly diagonalizing H_0 gives the eigenvectors:

$$v_1 = \begin{pmatrix} a \\ b \\ 1 \\ 0 \end{pmatrix}, v_2 = \begin{pmatrix} c \\ d \\ 0 \\ 1 \end{pmatrix}, v_3 = \begin{pmatrix} e \\ f \\ 1 \\ 0 \end{pmatrix}, v_4 = \begin{pmatrix} g \\ h \\ 0 \\ 1 \end{pmatrix} \quad (12)$$

Where the states (v_1, v_2) and (v_3, v_4) have pairwise the same eigenvalues, and the coefficients are complicated functions of the free parameters. These are not block diagonal as H_0 is not block diagonal. We could now in principle investigate which of these four states remain regular at the boundary, given some boundary conditions, and then project the perturbation H_1 in this basis. Note, however, that the resulting expression will be rather convoluted, with many free parameters. As we are only interested in the surface dispersion to compute the DOS, we choose to instead build a model for the surface directly.

B. Building the surface model directly

The surface close to the TRIM \bar{Z} exhibits time-reversal symmetry. Inversion symmetry is broken at the surface. However, there will be some residual effects of inversion symmetry, as otherwise H_0 should contain more terms, coming from the commutators of the Γ -matrices. Thus, inversion symmetry is broken down to some effective symmetry on the surface. The exact nature of this symmetry will depend on the orbital contents. Note in particular that if inversion acted purely as an effective C_2 symmetry, taking $(k_y, k_z) \rightarrow (-k_y, -k_z)$, then our

expansion in equation 18 in the main text would be trivial. The exact nature of this effective symmetry can be elucidated by solving the full bulk Hamiltonian above. For our purposes, however, it suffices to ignore this residual symmetry, and only focus on the time-reversal symmetry. The residual inversion symmetry will only constrain the form of our effective Hamiltonian further, potentially resulting in less free parameters. Thus, we do not lose any physical solutions by only ignoring the residual inversion symmetry, though we may find an unphysical parameter combination. As we are only interested in the shape of the surface dispersion, this is of no concern.

The time-reversal symmetry $\Theta = i\sigma_y\mathcal{K}$ acts in spin space on the surface by constraining:

$$H(\mathbf{k}) = (i\sigma_y)H^*(-\mathbf{k})(i\sigma_y)^{-1} \quad (13)$$

We can write a two-band model for the surface states as:

$$H(\mathbf{k}) = d(\mathbf{k}) \cdot \sigma \quad (14)$$

Hermiticity then requires that $d(\mathbf{k})$ should be real. Imposing time-reversal symmetry gives:

$$d_0(\mathbf{k}) = d_0(-\mathbf{k}), \quad d_1(\mathbf{k}) = -d_1(-\mathbf{k}), \quad d_2(\mathbf{k}) = -d_2(-\mathbf{k}), \quad d_3(\mathbf{k}) = -d_3(-\mathbf{k}) \quad (15)$$

With energy given by:

$$E(k) = d_0 \pm \sqrt{d_1^2 + d_2^2 + d_3^2} \quad (16)$$

Expanding to second order then gives:

$$H_2(k) = (E_0 + A_1k_y^2 + A_2k_z^2 + A_3k_yk_z)I + (B_1k_y + C_1k_z)\sigma_x + (B_2k_y + C_2k_z)\sigma_y + (B_3k_y + C_3k_z)\sigma_z \quad (17)$$

With energy

$$E_{2\pm}(k) = E_0 + A_1k_y^2 + A_2k_z^2 + A_3k_yk_z \pm \sqrt{\sum_{i=1}^3 (B_ik_y + C_ik_z)^2} \quad (18)$$

If we want to account for strain, we should expand to third order which gives an effective model:

$$\begin{aligned} H_3(k) = & (E_0 + A_1k_y^2 + A_2k_z^2 + A_3k_yk_z)I + (B_1k_y + C_1k_z + D_1k_y^2k_z + E_1k_z^2k_y)\sigma_x \\ & + (B_2k_y + C_2k_z + D_2k_y^2k_z + E_2k_z^2k_y)\sigma_y + (B_3k_y + C_3k_z + D_3k_y^2k_z + E_3k_z^2k_y)\sigma_z \end{aligned} \quad (19)$$

With energy:

$$E_{3\pm}(k) = E_0 + A_1k_y^2 + A_2k_z^2 + A_3k_yk_z \pm \sqrt{\sum_{i=3}^3 (B_ik_y + C_ik_z + D_ik_y^2k_z + E_ik_z^2k_y)^2} \quad (20)$$

Note that our energy is symmetric under $(k_y, k_z) \rightarrow (-k_y, -k_z)$ even though the Hamiltonian is not. This explains the observed effective C_2 symmetry in the FS.

The free parameters are fit using simulated annealing. This gives the result shown in table I and II.

A_1	A_2	A_3	B_1	C_1	B_2	C_2	B_3	C_3
1.779	3.827	0.886	-0.248	-1.225	-0.138	-0.252	0.185	0.273

TABLE I. Fit parameters for $E_{2\pm}$, see equation 18

A_1	A_2	A_3	B_1	C_1	D_1	E_1	B_2	C_2	D_2	E_2	B_3	C_3	D_3	E_3
1.895	8.051	2.701	0.145	0.021	-41.264	-150.345	0.082	-0.154	-2.524	-34.948	0.330	1.731	33.890	160.426

TABLE II. Fit parameters for $E_{3\pm}$, see equation 20

APPENDIX C: DFT CALCULATION OF 2D CUTS

Although the triclinic structure of RhBi₂ only has inversion symmetry, $\mathbf{k} \rightarrow -\mathbf{k}$, when projected on the (100) surface, the inversion symmetry in 2D gives an effective twofold rotation symmetry. This can also be understood in the 2D cuts of the 3D FS as shown in Fig. 6

2D Bulk FS Cuts along k_1

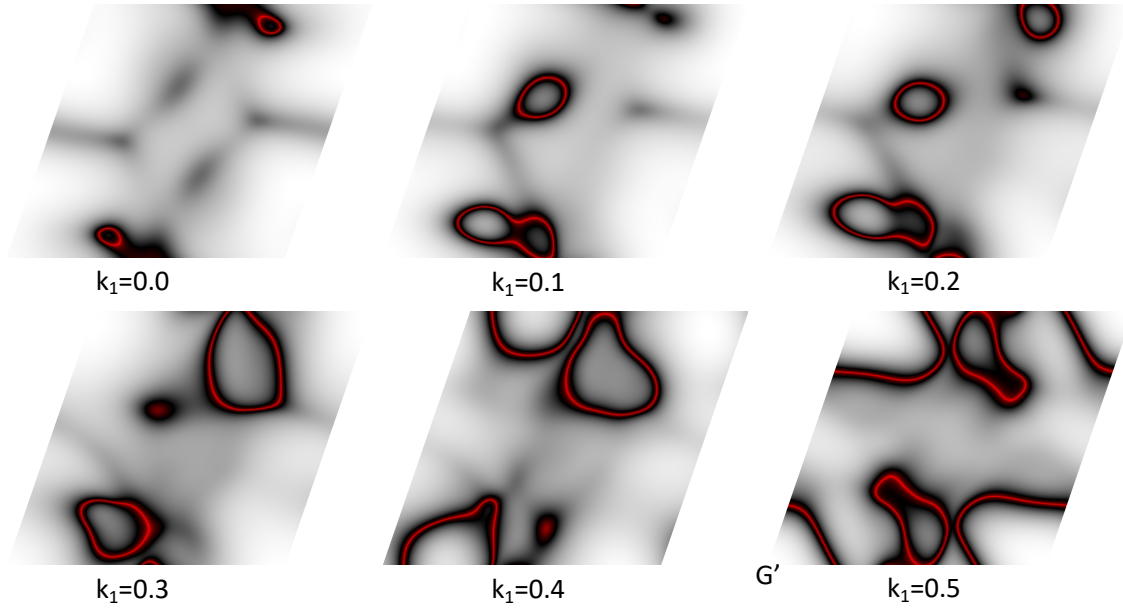


FIG. 6. **FS projection along k_1 direction** 2D bulk Fermi surface cuts for RhBi2 along $k_1=0.0$, 0.1, 0.2, 0.3, 0.4 and 0.5 planes. The 2-fold rotation symmetry only appears on the $k_1=0.0$ and 0.5 planes.

APPENDIX D: BAND STRUCTURE

A saddle point in the dispersion is characterized by a vanishing gradient, $\nabla\varepsilon_{\mathbf{k}} = 0$, and by opposite curvatures along orthogonal directions away from the extremum. Our ARPES measurements show evidence of the presence of a saddle point around the \bar{Z} point in the surface Brillouin zone (sBZ) of RhBi₂. To precisely determine the position of the saddle point, we perform a close investigation of the band structure using an effective low energy $k \cdot p$ model valid close to \bar{Z} .

A first look into the band structure of the $k \cdot p$ model suggest the existence of two saddle points in the SBZ [see Fig.4 (a)]. Interestingly, as shown in Fig.7, the lower band $\varepsilon_{-, \mathbf{k}}$ is almost flat along the diagonal direction parametrized by

$$k_y = k_{\bar{Z},y} + \alpha(k_z - k_{\bar{Z},z}) , \quad (21)$$

where $\alpha \approx 4.15$ and $(k_{\bar{Z},y}, k_{\bar{Z},z}) \approx (0, 0.5)\frac{\pi}{a}$, denotes the position the \bar{Z} point. Zooming into the region around \bar{Z} clearly shows two local minima along this flat direction at $(k_y - k_{\bar{Z},y}, k_z - k_{\bar{Z},z}) = \pm(-0.042, 0.010)\frac{\pi}{a} \equiv \pm\mathbf{k}_0$. These points, on the other hand, behave as local maxima of the dispersion along the direction orthogonal to Eq. (21). This behavior is evidenced in Figs. 8(a) and (b), respectively.

In fact, the gradient of the lower band $\nabla\varepsilon_{-, \mathbf{k}}$ vanishes at $\pm\mathbf{k}_0$ [see Figs.8(c) and (d)], which makes these points true saddle points of the lower band. They occur at energy $E = -83$ meV, where the peak in the surface density of states occurs [see Fig.4 (a)].

I. GAP EQUATION

In this section, we provide details on the analytic solution of the gap equation (5) in the main text in the presence of a logarithmically divergent density of states $\rho(\xi) = \rho_0 \log(D/|\xi|)$. After the change of variables $y = \xi/T_c$, the gap equation can be rewritten as

$$1 = g\rho_0 \int_0^{\Lambda/T_c} dy \log\left(\frac{D/T_c}{y}\right) \frac{1}{y} \tanh\left(\frac{y}{2}\right) . \quad (22)$$

Using properties of the logarithm, this integral can be further divided into two contributions,

$$\frac{1}{g\rho_0} = \log\left(\frac{D}{T_c}\right) \int_0^{\Lambda/T_c} dy \frac{1}{y} \tanh\left(\frac{y}{2}\right) - \int_0^{\Lambda/T_c} dy \frac{\log(y)}{y} \tanh\left(\frac{y}{2}\right) . \quad (23)$$

The first integral in the right-hand-side of Eq.(23) is identical to the one encountered in the standard BCS gap equation when approximating the DoS by its (constant) value at the Fermi level:

$$\int_0^{\Lambda/T_c} dy \frac{1}{y} \tanh\left(\frac{y}{2}\right) = \log\left(\frac{\kappa\Lambda}{T_c}\right), \quad (24)$$

where $\kappa = 2e^\gamma/\pi \approx 1.13$, and γ is Euler's constant. For the second integral in Eq.(23), a simple integration by parts yields

$$\int_0^{\Lambda/T_c} dy \frac{\log(y)}{y} \tanh\left(\frac{y}{2}\right) = \frac{1}{2} \log^2\left(\frac{\Lambda}{T_c}\right) - \frac{1}{4} \int_0^{\Lambda/T_c} dy \log^2(y) \operatorname{sech}^2\left(\frac{y}{2}\right). \quad (25)$$

Since $\Lambda/T_c \gg 1$ and $\log^2(y) \operatorname{sech}^2(y/2)$ remains finite as $y \rightarrow \infty$, we can approximate

$$\int_0^{\Lambda/T_c} dy \log^2(y) \operatorname{sech}^2\left(\frac{y}{2}\right) \approx \int_0^\infty dy \log^2(y) \operatorname{sech}^2\left(\frac{y}{2}\right) \approx \mathcal{C}, \quad (26)$$

where $\mathcal{C} = 2.669$ is a numerical constant. Substituting Eqs.(24) and (26) into Eq.(23), we

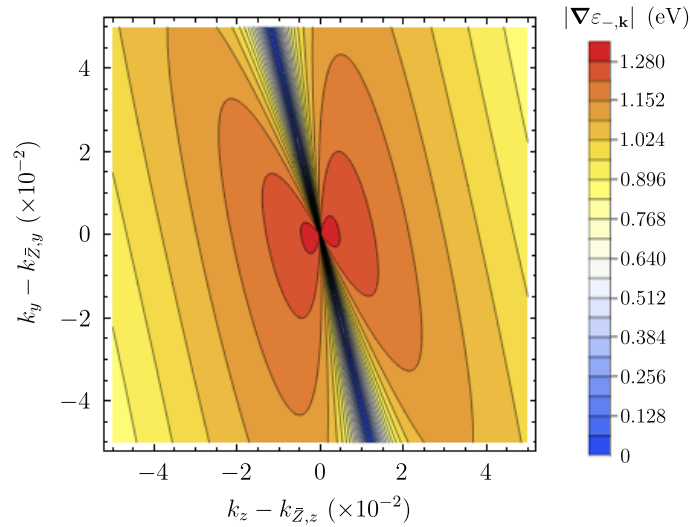


FIG. 7. **Gradient of the lowest energy band of the $k \cdot p$ model.** The direction where the norm of the gradient is minimum corresponds to the diagonal $k_y - k_{\bar{z},y} = -4.15 (k_z - k_{\bar{z},z})$. In particular, it vanishes at $(k_{y0}, k_{z0}) = \pm(-0.042, 0.010) \frac{\pi}{a}$ with respect to \bar{Z} . These are saddle points of the lowest energy band. The momenta k_y and k_z are given in units of π/a . Accordingly, $|\nabla\varepsilon_{-,k}|$ has dimensions of energy.

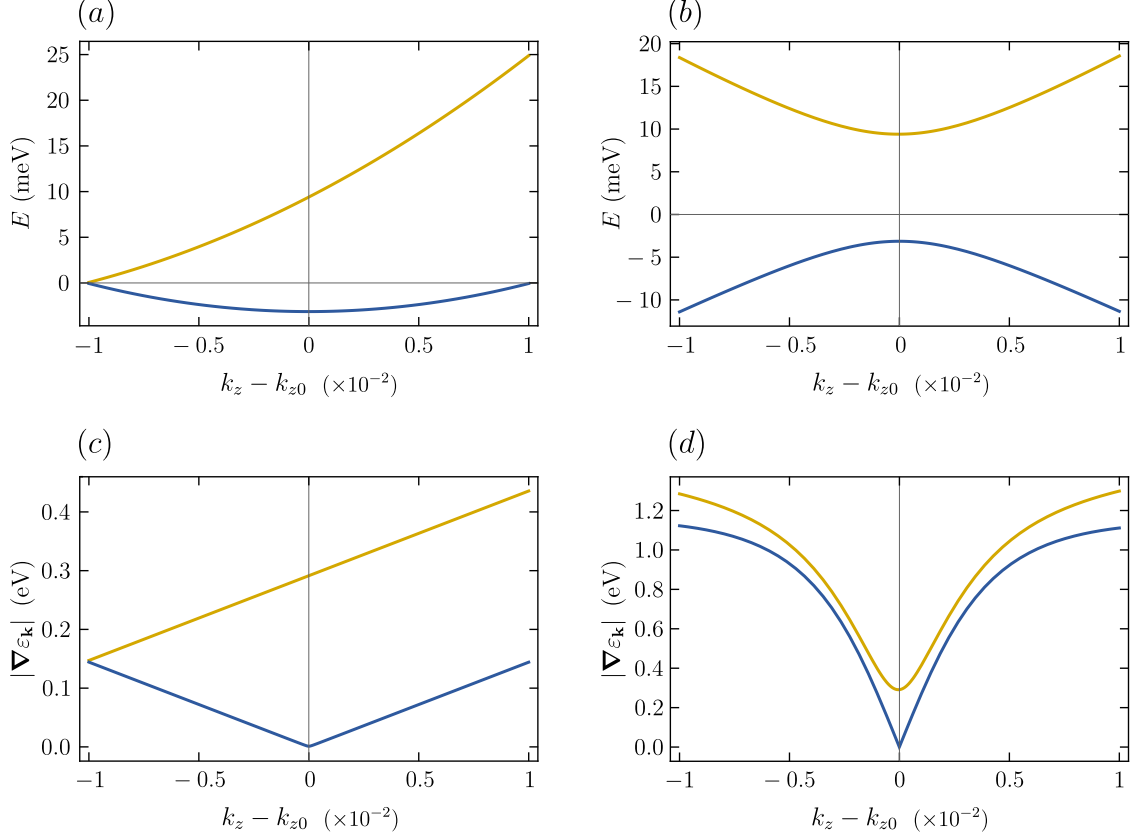


FIG. 8. Cuts of the band structure of the $k \cdot p$ model along the direction (a) $k_y - k_{\bar{z},y} = -4.15(k_z - k_{\bar{z},z})$ and the orthogonal direction (b) $k_y - k_{\bar{z},y} = 0.24(k_z - k_{\bar{z},z})$. Upper (lower) band is shown in yellow (blue). The dispersion is centered at the saddle point $\mathbf{k}_0 = (-0.042, 0.010)\frac{\pi}{a}$. Panels (c) and (d) show the norm of the gradient $|\nabla \varepsilon_{\mathbf{k}}|$ of the dispersion in **a** and **b**, respectively. The momenta k_y and k_z are given in units of π/a . Accordingly, $|\nabla \varepsilon_{\mathbf{k}}|$ has dimensions of energy.

obtain

$$\frac{1}{g\rho_0} = \log\left(\frac{D}{T_c}\right) \log\left(\frac{\kappa\Lambda}{T_c}\right) - \frac{1}{2} \log^2\left(\frac{\Lambda}{T_c}\right) + \frac{\mathcal{C}}{4}. \quad (27)$$

Since typically we have $D > \Lambda^{36}$, it is convenient to rewrite the logarithms in Eq.(27) in terms of D/T_c rather than Λ/T_c . This simplifies Eq.(27) significantly, since the linear term in $\log(\kappa D/T_c)$ vanishes identically. We thus find

$$\frac{2}{g\rho_0} = \log^2\left(\frac{\kappa D}{T_c}\right) + \frac{\mathcal{C}}{2} - \log^2\left(\frac{\Lambda}{D}\right) - \log^2\left(\frac{1}{\kappa}\right). \quad (28)$$

The strongest divergence comes from the term $\log^2(\kappa D/T_c)$, so that we can neglect the three last terms in the right-rand-side of Eq.(28), which yields T_c as given in Eq.(6) of the main text.